bioRxiv preprint doi: https://doi.org/10.1101/459412; this version posted November 1, 2018. The copyright holder for this preprint (which was not certified by peer review) is the author/funder, who has granted bioRxiv a license to display the preprint in perpetuity. It is made available under aCC-BY-NC 4.0 International license.

Discrete Mechanical Growth Model for Plant Tissue

Louis D. Weise, Kirsten H. W. J. ten Tusscher
Department of Biology, Utrecht University, Utrecht, the Netherlands
∗ E-mail: Louis.Daniel.Weise@gmail.com

Abstract

We present a discrete mechanical model to study plant development. The method is built up of mass points, springs and hinges mimicking the plant cell wall's microstructure. To model plastic growth the resting lengths of springs are adjusted; when springs exceed a threshold length, new mass points, springs and hinges, are added. We formulate a stiffness tensor for the springs and hinges as a function of the fourth rank tensor of elasticity and the geometry of the mesh. This allows us to approximate the material law as a generalized orthotropic Hooke's law, and control material properties during growth. The material properties of the model are illustrated in numerical simulations for finite strain and plastic growth. To solve the equations of motion of mass points we assume elastostatics and use Verlet integration. The method is demonstrated in simulations when anisotropic growth causes emergent residual strain fields in cell walls and a bending of bulk tissue. The method can be used in multilevel models to study plant development, for example by coupling it to models for cytoskeletal, hormonal and gene regulatory processes.

Introduction

Plant development is a complex process, it self-organizes using hormonal, gene regulatory and mechanical processes that act on multiple length- and time-scales and are linked via feedback loops. For instance, active and passive transport of hormones affects gene expression, but is also controlled by it: e.g. the hormone auxin [1] affects the expression of its own transport proteins [2], while also the expression of those transporters regulates the distribution of auxin [3]. Moreover, gene regulatory and hormonal processes govern the plant's mechanical processes [4, 5], such as the cell wall's expansive growth, rupture, and cell division. However, also mechanical determinants feed back on genetical and hormonal processes [6, 7]. For instance, auxin guides root growth [8, 9], while a bending of the root also causes changes in auxin patterning [10, 11].

It is difficult to understand the consequences of such feedback loops from experiments alone. This is because experimental measurements are typically limited in their spatial and temporal scope, as well as in the number of processes that can be studied simultaneously. Mathematical modeling has been shown to be a valuable tool to study complex biological systems compassed of processes happening on different time- and length- scales and involving feedback loops [12, 13]. As a consequence, joint experimental and modeling approaches have led to important insights in plant development [8, 10, 14, 15].

There exist numerous models for plant growth that qualitatively capture tissue deformation due to growth, but do not reflect elastic properties (e.g.: [16–18]). However, plants are sensing those mechanical clues and are responding to them [19]. For instance, during cell division when a new cell wall is built, it is oriented such that it optimally resists tensile stress [20]. Also plant cells reinforce their wall by adding new microfibrils in the orientation of the highest stress [21]. Therefore mathematical models for plant growth need to be developed that include elastic properties.

It is challenging to develop such models for plant growth mechanics since plant tissue is a complex material that can be highly anisotropic and undergoes both elastic and plastic deformations during

bioRxiv preprint doi: https://doi.org/10.1101/459412; this version posted November 1, 2018. The copyright holder for this preprint (which was not certified by peer review) is the author/funder, who has granted bioRxiv a license to display the preprint in perpetuity. It is made available under aCC-BY-NC 4.0 International license.

development. Plant cells are typically under a high turgor pressure, while being encased in stiff cell walls that resist this pressure [22]. Dynamical regulation (genetically and hormonally controlled) of the cell wall's stiffness allows plastic growth [23], as well as the more extensive cell wall remodelling that is for example necessary for lateral root emergence [24].

The most established way to model the mechanics of plant development is in terms of continuum mechanics [25, 26]. The application of continuous mechanical models has resulted in important insights, for example the demonstration that mechanical signals together with auxin patterning synergystically regulate plant shoot morphogenesis [15, 27]. A main advantage of the continuum mechanics approach is that material properties of the tissue are implicitly maintained during deformation, which is important since stress- and strain fields are relevant for plant morphogenesis [20, 27]. However, continuous methods have also theoretical and practical limitations. The plant's cell wall is inherently discrete, consisting of networks of crosslinked fibrils. Mechanical processes on this scale, such as stiffening, loosening or rupture of fibrils are important for plant development (e.g. during lateral root formation), but are difficult to access locally with continuous models. Technically, it is a challenging problem to implement a continuum mechanics approach in a computationally efficient manner.

Discrete mechanical modeling offers an interesting alternative to continuum mechanics. A discrete mechanical model can mimic the microstructure of the plant's cell wall, while typically being more computationally efficient to solve. However, a main drawback of discrete mechanical models is that material properties are most often not well defined: typically relations between discrete mass points are described, yet the stress-strain relation is not explicitly formulated [28]. Furthermore, deformations, e.g. due to growth, change the geometry of the mesh, thus causing undesired changes in material properties. In this paper we develop a discrete mechanical model to study plant development that is aimed at alleviating these limitations. We formulate a stiffness tensor for the mass point's springs and hinges in terms of a generalized orthotropic Hooke's law and the geometry of the mesh. Furthermore, we develop a remeshing method to control the mass point density and material properties during growth. Our model enables the incorporation of experimental data on elastic properties of plant cell walls. Finally, given the discrete nature of the model we can affect the stiffness of cell wall components in a localized manner.

We demonstrate the model in simulations on anisotropic tissue growth. The model allows us to study strain fields and tissue bending that emerge due to anisotropic growth. The method can be coupled to existing models for hormone and gene regulatory networks and thus provides a valuable building block for multilevel models of plant development. The advantage of computational efficiency and numerical simplicity make our model an attractive method for researchers studying development of tissues involving growth mechanics of turgoid cells.

Methods

Main assumptions

First, we explain our main working assumptions: reduction of dimensionality, and usage of a simplified material law, before we explain the setting up of the model.

Reduction of dimensionality: plane stress assumption

Plant tissues are inherently three-dimensional. However, for many important research questions it is often reasonable to approximate plant tissue using simplified two-dimensional (2D) models. For instance, it has been shown in a 2D model that root bending may cause maxima in local auxin production [10]. Indeed, previous models for plant growth have used a 2D approximation, for instance the vertex- and

bioRxiv preprint doi: https://doi.org/10.1101/459412; this version posted November 1, 2018. The copyright holder for this preprint (which was not certified by peer review) is the author/funder, who has granted bioRxiv a license to display the preprint in perpetuity. It is made available under aCC-BY-NC 4.0 International license.

hybrid vertex-midline models of Fozard et al. [17,18] and Merks et al. [16]. A 2D approximation using the plane stress assumption is often made in shell models for plant tissue [27, 29]. The rationale behind this simplification comes from the observation that the cell walls of the outer cell layer (epidermis) of plant tissue is typically stiffer than its inner ones, and basically acts as a "tension-stressed skin" [30, 31]. Here we also make use of the plane stress assumption to build a mechanical growth model for plant tissue.

Simplified material properties

Elastic properties of a material are formulated in terms of constitutive relations, equations that connect stress and strain. Constitutive relations of plant tissues are complex, as these tissues are typically anisotropic, and consist of distinct cell layers with divergent mechanical properties [32]. Furthermore, these properties are changing dynamically. For example, it has been shown that the stiffness of cell walls of *Arabidopsis thaliana* varies over one order of magnitude depending on the growth phase [33]. While there are powerful methods to measure material properties of living plant tissue [34,35], to our knowledge, so far only linear relationships between stress and strain have been measured. Therefore we use in our model a linear relationship between stress and strain and neglect higher order terms.

Elastic model

Here we describe the setup of the discrete elastic model. We start with illustrating the mesh of the model which is built up by mass points, springs and hinges. For the springs and hinges we formulate a stiffness tensor in terms of the geometry of the mesh and the elasticity tensor. Then we explain how we describe elastic anisotropy and turgor pressure. Next we formulate an approximate material law. Finally we explain how we calculate the forces on mass points.

Mesh

We use a square lattice, where every mass point has four (if not at the border) neighboring mass points connected by springs (Figure 1A). A unit cell in this crystal lattice is shown in Figure 1B. In addition to

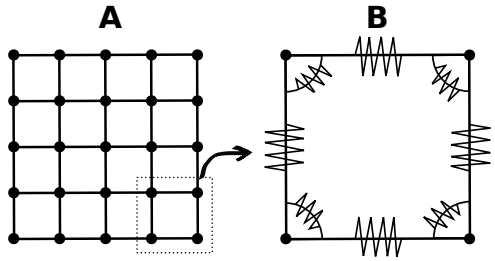

Figure 1. (A) Mechanical mesh. Dots indicate mass points. Springs are indicated as lines. Dotted contour indicates inset for subfigure. **(B) Unit cell**. Springs are indicated by zigzagging lines on straight lines. Zigzagging lines on curved lines connecting horizontal and vertical springs indicate hinges.

springs to direct neighbors, there are hinges in each corner of a unit cell. The rationale for choosing this layout of mass points, springs and hinges is as follows. Plant tissues such as the root tip or hypocotyl are often anisotropic, and this anisotropy is caused by the presence of polarized cells. In these polarized cell types there are two principal cellulose fiber directions, one along the growth direction, and one perpendicular to it [36]. In contrast, some plant tissues are isotropic, containing apolar cells in which the cellulose fiber mesh is disoriented. Since we are interested in modeling plant tissues consisting of

bioRxiv preprint doi: https://doi.org/10.1101/459412; this version posted November 1, 2018. The copyright holder for this preprint (which was not certified by peer review) is the author/funder, who has granted bioRxiv a license to display the preprint in perpetuity. It is made available under aCC-BY-NC 4.0 International license.

polarized cells, we choose a quadratic unit cell to mimic the two principal fiber directions of polar plant cells.

Coupling to a continuous material law

The elastic properties of our model are determined by the geometry of the lattice unit cell and the stiffness of the springs and hinges. Here we will formulate these microscopic properties in the continuum limit from the macroscopic elastic properties of a linear elastic material.

The elastic energy density Ψ of a linear elastic material [37] is given by

$$\Psi = \frac{1}{2}\sum_{ijkl} C_{ijkl}\varepsilon_{ij}\varepsilon_{kl}, \tag{1}$$

where C_{ijkl} are elements of the elasticity tensor, and ε_{ij} are components of the small strain tensor $\boldsymbol{\epsilon}$. For an isotropic material the above simplifies to

$$\Psi = \frac{1}{2}\left(\lambda\left(\sum_k \varepsilon_{kk}\right)^2 + 2\mu\sum_{ij}\varepsilon_{ij}^2\right), \tag{2}$$

where λ and μ are the Lamé coefficients. The elements σ_{ij} of Cauchy's stress tensor $\boldsymbol{\sigma}$ can be obtained (assuming constant temperature) by differentiating Ψ with respect to components from the strain tensor [38]

$$\sigma_{ij} = \frac{\partial\Psi}{\partial\varepsilon_{ij}}. \tag{3}$$

Substituting Ψ with Eq.2 we obtain the generalized Hooke's law

$$\sigma_{ij} = \lambda\left(\sum_k \varepsilon_{kk}\right)\delta_{ij} + 2\mu\varepsilon_{ij}, \tag{4}$$

where δ_{ij} is the Kronecker delta.

To formulate a stiffness tensor for springs and hinges in terms of Lamé coefficients, we will take the following approach. First a description of the elastic energy density for the discrete model in terms of Lamé coefficients and the geometry of the mesh is found. Then we will do the same as above, find the elements of the stress tensor by deriving the elastic energy density with respect to strain elements. Finally, we will compare the elastic energy density and stress tensor descriptions of our model to Eq.4 and Eq.1.

For the elastic potential of a spring in the x-direction we use $(1/2)k(x_0/y_0)\Delta x^2$, with spring stiffness k, and $\Delta x = x - x_0$ the change of length of a horizontal spring, where x is the actual length (see Appendix **A1** [39]), and x_0 is its resting length (similar terminology for the y-direction). We will use the potential $(1/2)k\Delta x\Delta y$ to account for the Poisson effect (compare e.g. component $\sigma_{yy} = C_{yyxx}\varepsilon_{yy}$ in Eq.4). Shear is described by means of four hinges per unit cell in terms of the potential $(1/8)\kappa\Delta D^2$ for each hinge, with κ the hinge stiffness, and ΔD the change of length of a diagonal in the unit cell. Figure 2 depicts a parallelogram which is used to formulate shear in terms of diagonals in a unit cell. Similarly to Eq.4 we write the elastic energy density $\tilde{\Psi}$ of the discrete mechanical model as

$$\tilde{\Psi} = \frac{E}{A} = \frac{1}{2A}\left[k\left(h\Delta x^2 + h^{-1}\Delta y^2 + 2\Delta x\Delta y\right) + \kappa\left(h\Delta x^2 + h^{-1}\Delta y^2 + 2\Delta D^2\right)\right], \text{ with: } h := x_0/y_0, \tag{5}$$

bioRxiv preprint doi: https://doi.org/10.1101/459412; this version posted November 1, 2018. The copyright holder for this preprint (which was not certified by peer review) is the author/funder, who has granted bioRxiv a license to display the preprint in perpetuity. It is made available under aCC-BY-NC 4.0 International license.

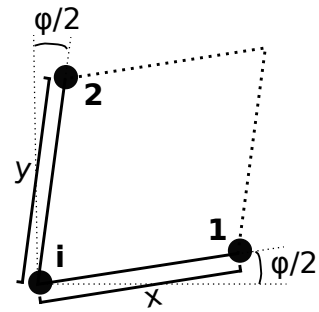

Figure 2. Illustration of parallelogram used to describe shear. To calculate forces on point $\boldsymbol{i}$ which results from one horizontal and vertical spring and one hinge the position of three mass points ($\boldsymbol{i}$,**1**,**2**) is used. We construct a parallelogram from these points (note thick dotted lines) to define shear.

where E is the elastic energy of an unit cell, and A is its surface area. One horizontal spring is shared between two unit cells, whereas each unit cell contains two horizontal springs. Therefore, the net longitudinal strain of a single unit cell can be described as the deformation of a single spring $\varepsilon_{xx} = \Delta x/x_0$. Total shear of a unit cell is defined [37] as $\tau := \tan\varphi$ (compare Figure 2), and the components of the shear strain tensor as $\varepsilon_{xy} = \varepsilon_{yx} := (1/2)\tau$. We find (see Figure 2 and Appendix **A2** [39])

$$2\Delta D^2 = 2\tilde{s}^2 D_0^2 \tau^2 = 4\tilde{s}^2 D_0^2(\varepsilon_{xy}^2 + \varepsilon_{yx}^2), \text{ with: } \tilde{s} := \frac{s}{1+s^2}, \text{ and: } s := \frac{\max(x_0, y_0)}{\min(x_0, y_0)}, \tag{6}$$

where $D_0 = \sqrt{x_0^2 + y_0^2}$ is the length of a diagonal of an undeformed unit cell. We rewrite $\tilde{\Psi}$ in terms of strain

$$\begin{aligned}\tilde{\Psi} = \frac{1}{2A}[k(hx_0^2\varepsilon_{xx}^2 + h^{-1}y_0^2\varepsilon_{yy}^2 + 2x_0\varepsilon_{xx}y_0\varepsilon_{yy}) + \\ \kappa\left(hx_0^2\varepsilon_{xx}^2 + h^{-1}y_0^2\varepsilon_{yy}^2 + 4\tilde{s}^2\left(x_0^2 + y_0^2\right)\left(\varepsilon_{xy}^2 + \varepsilon_{yx}^2\right)\right)]\end{aligned} \tag{7}$$

To get the elements of the stress tensor we differentiate $\tilde{\Psi}$ with respect to strain. We approximate

$$\sigma_{ij} = \frac{\partial\tilde{\Psi}}{\partial\varepsilon_{ij}} = \frac{E'}{A} - \frac{A'E}{A^2} \approx \frac{E'}{A} \text{ (for small strain – see Appendix } \mathbf{B} \text{ [39])}, \tag{8}$$

and compare the resulting expressions with Eqs.4 and 1 to get

$$C_{xxxx} = \lambda + 2\mu \mathrel{\widehat{=}} (k+\kappa)\, hx_0^2/A \tag{9a}$$

$$C_{yyyy} = \lambda + 2\mu \mathrel{\widehat{=}} (k+\kappa)\, h^{-1}y_0^2/A \tag{9b}$$

$$C_{xxyy} = C_{yyxx} = \lambda \mathrel{\widehat{=}} kx_0y_0/A \tag{9c}$$

$$C_{xyxy} = C_{yxyx} = 2\mu \mathrel{\widehat{=}} \kappa 4\tilde{s}^2\left(x_0^2 + y_0^2\right)/A. \tag{9d}$$

The stiffness tensor of the discrete mechanical model $\tilde{C}_{ijkl}$ can now be written in terms of Lamé coefficients and geometric properties of an unit cell (we replace k and κ)

$$\tilde{C}_{xxxx} := (\lambda + 2\mu)\, h^{-1}A/x_0^2 \tag{10a}$$

$$\tilde{C}_{yyyy} := (\lambda + 2\mu)\, hA/y_0^2 \tag{10b}$$

$$\tilde{C}_{xxyy} = \tilde{C}_{yyxx} := (\lambda)\, A/x_0y_0 \tag{10c}$$

$$\tilde{C}_{xyxy} = \tilde{C}_{yxyx} := (2\mu)\, A/\left((x_0^2 + y_0^2)4\tilde{s}^2\right) \tag{10d}$$

$$\text{other components} := 0. \tag{10e}$$

bioRxiv preprint doi: https://doi.org/10.1101/459412; this version posted November 1, 2018. The copyright holder for this preprint (which was not certified by peer review) is the author/funder, who has granted bioRxiv a license to display the preprint in perpetuity. It is made available under aCC-BY-NC 4.0 International license.

Finally, $\tilde{\Psi}$ can be expressed similarly to Eq.1 as

$$\tilde{\Psi} = \frac{1}{2} \sum_{ijkl} \tilde{C}_{ijkl} \varepsilon_{ij} \varepsilon_{kl}, \tag{11}$$

Anisotropy

In many plant tissues, cells are mechanically anisotropic. This is partly because of tissue specific polarized orientation of cellulose microfibrils in their cell walls [32]. To account for anisotropy we define two Young's moduli, one for the x-direction Y_x, and one for the y-direction Y_y. In plane stress Lamé coefficients are connected to Young's moduli and Poisson's ratio ν [40] via

$$\lambda_x = \frac{Y_x \nu}{1-\nu^2}, \quad \mu_x = \frac{Y_x}{2(1+\nu)} \tag{12a}$$

$$\lambda_y = \frac{Y_y \nu}{1-\nu^2}, \quad \mu_y = \frac{Y_y}{2(1+\nu)} \tag{12b}$$

We define the shear modulus μ as the mean of the shear moduli of the isotropic materials characterized by either Young's modulus (Y_x, ν) and (Y_y, ν)

$$2\mu := \mu_x + \mu_y := \frac{Y_x + Y_y}{2(1+\nu)}. \tag{13}$$

We rewrite the stiffness tensor $\tilde{C}_{ijkl}$ (Equation 10) for the anisotropic model

$$\tilde{C}_{xxxx} = (\lambda_x + 2\mu_x)\, h^{-1} A / x_0^2 \tag{14a}$$

$$\tilde{C}_{yyyy} = (\lambda_y + 2\mu_y)\, h A / y_0^2 \tag{14b}$$

$$\tilde{C}_{xxyy} = (\lambda_x)\, A / x_0 y_0 \tag{14c}$$

$$\tilde{C}_{yyxx} = (\lambda_y)\, A / x_0 y_0 \tag{14d}$$

$$\tilde{C}_{xyxy} = \tilde{C}_{yxyx} = (\mu_x + \mu_y)\, A / \left((x_0^2 + y_0^2) 4 \tilde{s}^2 \right). \tag{14e}$$

Constitutive relations

In the derivations presented above the small strain tensor ϵ was used to derive the properties of the springs and hinges. However, the small strain tensor is not invariant to rigid body rotations, and is thus not suitable to describe a finite elastic material [41]. In continuum mechanics we would need to apply a polar decomposition first, to cancel out rigid body rotations and obtain the Biot strain tensor. However, in our case, we do this implicitly, because we define strain in terms of relative length changes of springs, and angles between them. Thus, in our model we are approximating the Biot strain tensor $\boldsymbol{e}$ (also called nominal strain) [42]. Biot strain is part of the Seth-Hill strain family [43], and a commonly used finite strain tensor.

With this we can approximate the elastic constitutive material relations for our anisotropic model as a generalized orthotropic Hooke's law

$$\begin{bmatrix} \sigma_{xx} \\ \sigma_{yy} \\ \sigma_{xy} \\ \sigma_{yx} \end{bmatrix} = \begin{bmatrix} 2\mu_x + \lambda_x & \lambda_x & 0 & 0 \\ \lambda_y & 2\mu_y + \lambda_y & 0 & 0 \\ 0 & 0 & \mu_x + \mu_y & 0 \\ 0 & 0 & 0 & \mu_x + \mu_y \end{bmatrix} \begin{bmatrix} e_{xx} \\ e_{yy} \\ e_{xy} \\ e_{yx} \end{bmatrix}. \tag{15}$$

bioRxiv preprint doi: https://doi.org/10.1101/459412; this version posted November 1, 2018. The copyright holder for this preprint (which was not certified by peer review) is the author/funder, who has granted bioRxiv a license to display the preprint in perpetuity. It is made available under aCC-BY-NC 4.0 International license.

Turgor pressure

Assuming that turgor pressure p_t is constant across the tissue, i.e. all cells are equally turgid, the hydrostatic potential E_{hp} caused by p_t is

$$E_{hp} = -A_t p_t, \tag{16}$$

with A_t being the surface area of the tissue.

Calculation of forces

In the following sections the calculation of the forces acting on the mass points will be explained. The forces will be used to compute the motion of the mass points.

Elastic forces

Elastic force on a mass point i (compare Figure 2) $\boldsymbol{f}_i^e$ is the negative gradient of the elastic energy E with respect to $\boldsymbol{i}$ (note: i is an index, $\boldsymbol{i}$ is position vector of mass point i)

$$\boldsymbol{f}_i^e = -\nabla_i E(e_{kl}(\boldsymbol{i})) = \sum_{kl} -\frac{\partial(A\tilde{\Psi})}{\partial e_{kl}} \frac{\partial e_{kl}}{\partial \boldsymbol{i}} \approx -A \sum_{kl} \sum_{no} \tilde{C}_{klno} e_{no} \frac{\partial e_{kl}}{\partial \boldsymbol{i}} \text{ (see Appendix } \mathbf{C} \text{ [39]).} \tag{17}$$

We expand it to (note that $e_{xy} = e_{yx} = (1/2)\tau$)

$$\boldsymbol{f}_i^e = -\left(\tilde{C}_{xxxx} e_{xx} + \tilde{C}_{xxyy} e_{yy}\right) A \frac{\partial e_{xx}}{\partial \boldsymbol{i}} \tag{18a}$$

$$-\left(\tilde{C}_{yyyy} e_{yy} + \tilde{C}_{yyxx} e_{xx}\right) A \frac{\partial e_{yy}}{\partial \boldsymbol{i}} \tag{18b}$$

$$-\left(\tilde{C}_{xyxy} \tau\right) A \frac{\partial e_{xy}}{\partial \boldsymbol{i}}. \tag{18c}$$

To solve Eq.18 we need to specify A and e_{ij} with respect to an individual mass point i, and get the derivatives $\partial e_{ij}/\partial \boldsymbol{i}$. Let us start with terms 18a,18b.

As can be seen from Figure 1A, a mass point inside the mesh is connected to four neighboring mass points and thus part of four unit cells (compare Figure 1B). A mass point at the boundary is part of two unit cells, and a point in the corner of only one unit cell. Therefore the mean surface area of the unit squares connected to the mass point i is used as variable A in terms 18a and 18b. Terms 18a,18b are calculated for all springs connected to mass point i. Thereby e_{xx} is the strain of one respective spring (similar in the y-direction). To calculate the force due to the Poisson effect, we use the strain in the "other direction", e.g. e_{yy} for a spring in x direction (see term $\tilde{C}_{xxyy} e_{yy}$), the mean e_{yy} strain of the adjacent springs in y-direction. Accordingly, we use the mean resting lengths of the adjacent springs in the y-direction to compute y_0 in $\tilde{C}_{xxyy}$. The derivatives of the direct strain elements with respect to coordinates of $\boldsymbol{i}$ are

$$\frac{\partial e_{xx}}{\partial \boldsymbol{i}} = -\frac{\boldsymbol{x}}{x_0 \|\boldsymbol{x}\|} \tag{19a}$$

$$\frac{\partial e_{yy}}{\partial \boldsymbol{i}} = -\frac{\boldsymbol{y}}{y_0 \|\boldsymbol{y}\|}. \tag{19b}$$

The term 18c is computed as follows:
the total shear force at a single mass point is described by its N adjacent hinges ($N = 4$ for a mass point

bioRxiv preprint doi: https://doi.org/10.1101/459412; this version posted November 1, 2018. The copyright holder for this preprint (which was not certified by peer review) is the author/funder, who has granted bioRxiv a license to display the preprint in perpetuity. It is made available under aCC-BY-NC 4.0 International license.

in the medium, $N = 2$ for a mass point at the boundary of the mesh, and $N = 1$ for a point in the corner of the mesh). We define total shear strain at a single mass point τ as the mean of it's N adjacent "hinge shear strains"

$$\tau := \frac{1}{N}\sum_{n=1}^{N}\tau_n \tag{20}$$

We use Figure 2 to illustrate how we calculate hinge shear strain τ_n for a hinge n. We use the springs in the x- and y-direction to define vectors: $\boldsymbol{x}_n := \mathbf{1} - \boldsymbol{i}$, $\boldsymbol{y}_n := \mathbf{2} - \boldsymbol{i}$ and use them to define τ_n

$$\tau_n := \tan\varphi = \tan(\arcsin(a_n)) = \frac{a_n}{\sqrt{1-a_n^2}}, \text{with: } a_n := \frac{\boldsymbol{x}_n \cdot \boldsymbol{y}_n}{\|\boldsymbol{x}_n\|\,\|\boldsymbol{y}_n\|}. \tag{21}$$

To calculate forces due to hinge shear strains in term 18c, we use the properties of the respective hinges: for the surface area of a unit cell we use $A_n := \|\boldsymbol{x}_n \times \boldsymbol{y}_n\|$ (compare surface area of parallelogram in Figure 2). We also use respective springs in x- and y-direction of each hinge, to replace $(x_0^2 + y_0^2)$ and $\tilde{s}$ in Equation 10d with the corresponding hinge properties $(x_{0(n)}^2 + y_{0(n)}^2)$ and $\tilde{s}_n$. With this we rewrite (see Appendix **D** [39]) the shear force acting at a mass point i (term 18c) as a sum over the adjacent hinges

$$-\left(\tilde{C}_{xyxy}\tau\right)A\frac{\partial e_{xy}}{\partial \boldsymbol{i}} = \frac{-\mu}{N}\sum_{n=1}^{N}\left[\frac{A_n^2}{\left(x_{0(n)}^2 + y_{0(n)}^2\right)4\tilde{s}_n^2}\frac{\tau_n\left(1+\tau_n^2\right)}{\sqrt{1-a_n^2}}\left(a_n\left(\frac{\boldsymbol{y}_n}{\|\boldsymbol{y}_n\|^2} + \frac{\boldsymbol{x}_n}{\|\boldsymbol{x}_n\|^2}\right) - \frac{(\boldsymbol{x}_n + \boldsymbol{y}_n)}{\|\boldsymbol{x}_n\|\,\|\boldsymbol{y}_n\|}\right)\right]. \tag{22}$$

Forces due to turgor pressure

A_t in Eq. 16 is a planar non-self-intersecting polygon with vertices described by the position of mass points at the border of the tissue $(x_1, y_1), ..., (x_n, y_n)$ (vertices listed counterclockwise), thus A_t is given [44] by

$$A_t = \frac{1}{2}\left(\begin{vmatrix} x_0 & x_1 \\ y_0 & y_1 \end{vmatrix} + \begin{vmatrix} x_1 & x_2 \\ y_1 & y_2 \end{vmatrix} + \cdots + \begin{vmatrix} x_{n-2} & x_{n-1} \\ y_{n-2} & y_{n-1} \end{vmatrix} + \begin{vmatrix} x_{n-1} & x_0 \\ y_{n-1} & y_0 \end{vmatrix}\right). \tag{23}$$

The "turgor force" $\boldsymbol{f}_i^t$ acting at a mass point i (if at the border of the medium), due to p_t is the negative gradient of the hydrostatic potential E_{hp} with respect to $\boldsymbol{i}$

$$\boldsymbol{f}_i^t = -\nabla_i E_{hp}(\boldsymbol{i}) \overset{(16,23)}{=} \frac{p_t}{2}\begin{bmatrix} y_{i+1} - y_{i-1} \\ -x_{i+1} + x_{i-1} \end{bmatrix}. \tag{24}$$

Viscous forces

We use a viscous force acting on every mass point to find the equilibrium configuration of the mesh

$$\boldsymbol{f}_i^d = -\eta\frac{d}{d\gamma}\boldsymbol{i}, \tag{25}$$

where η is the damping constant, and γ is the dimensionless integration time of the elasticity part of the model (see following section "Elastostatics" and "Numerical Methods").

Elastostatics

The motion of the mass points is described by Newton's law of motion

$$\boldsymbol{f}_i = \boldsymbol{f}_i^e + \boldsymbol{f}_i^d + \boldsymbol{f}_i^t = m\frac{d^2}{d\gamma^2}\boldsymbol{i}, \tag{26}$$

bioRxiv preprint doi: https://doi.org/10.1101/459412; this version posted November 1, 2018. The copyright holder for this preprint (which was not certified by peer review) is the author/funder, who has granted bioRxiv a license to display the preprint in perpetuity. It is made available under aCC-BY-NC 4.0 International license.

where parameter m is the mass of a mass point.

We make the common assumption [29] that deformations happen at mechanical equilibrium. This can be understood from the fact that the plant's growth processes are much slower than its elastic response to external forces. By solving Eq. 26 until mechanical equilibrium ($\boldsymbol{f}_i = 0$) we find the steady state configuration of the lattice. Note that the mass of a mass point m and the viscosity η have no physical relevance in this model, as they do not affect the equilibrium configuration of the mesh. These parameters only fulfill numerical roles (convergence rate and precision).

Plastic growth

Irreversible plant growth arises through the elongation of cell-walls of individual cells. This process involves cell wall loosening, expansion of the cell, and addition of new cell wall material restoring original cell wall stiffness [45].

In the present paper we will apply our model to study basic effects of anisotropic growth such as emergence of residual strains and bulk deformation. To model growth the resting length of springs is adjusted

$$\frac{d}{dt}\begin{bmatrix} x_0 \\ y_0 \end{bmatrix}(t, \text{position}) = \begin{bmatrix} k_x^{rate} \\ k_y^{rate} \end{bmatrix}(t, \text{position}) \begin{bmatrix} x_0 \\ y_0 \end{bmatrix}(t, \text{position}), \tag{27}$$

where t is the simulation time, and $k_x^{rate}(t)$ is the growth rate of a spring in the x-direction (similar terminology for the y-direction). This approach is similar to an evolving metric in the material manifold [46], and has been used before in a continuous mechanical growth model for plant tissue [29].

Remeshing

The mass point density is affected by the growth process. Therefore, when springs exceed a threshold length of $\sqrt{2}\times$(initial spring length), we add new mass points, springs and hinges to mimic the deposition of new cell wall material accompanying the later stages of cell expansion. We do this via the algorithm depicted in Figure 3. It can be seen from Figure 3 that "loose mass points" can emerge in the medium during growth, points that have only three instead of four neighbors. We will see later in the results section that such loose points emerge when anisotropic growth causes triggering of remeshing in locally while neighboring regions are not remeshed. However, we still calculate four hinge strains (see Eq.21) for such a loose point. For this an auxiliary point (see Figure 4) is assumed Note that we do not calculate forces on auxiliary points. We calculate vector $\boldsymbol{y}$ using the loose mass point's coordinates and the coordinates of the auxiliary point (similar for $\boldsymbol{x}$ when a loose end is pointing sideways). As resting distance y_0 the resting distance of the left neighbor is used (similar, when a loose end is pointing sideways x_0 of the upper neighbor is used).

Numerical methods

We solved the equations of our model by combining explicit Euler integration for the growth equation Eq. 27, and Verlet integration [47] to solve the equations for the motion of the mass points Eqs. 26.

The position of a mass point $\boldsymbol{i}$ at integration time $\gamma + h\gamma$ is computed with

$$\boldsymbol{i}(\gamma + h\gamma) = 2\boldsymbol{i}(\gamma) - \boldsymbol{i}(\gamma - h\gamma) + \frac{d^2}{d\gamma^2}\boldsymbol{i}(\gamma) \times (h\gamma)^2,$$

bioRxiv preprint doi: https://doi.org/10.1101/459412; this version posted November 1, 2018. The copyright holder for this preprint (which was not certified by peer review) is the author/funder, who has granted bioRxiv a license to display the preprint in perpetuity. It is made available under aCC-BY-NC 4.0 International license.

FOR each vertical spring:
  IF spring is longer than √2 * (initial length), **THEN:**
    add new mass point in middle of spring; split spring into two:

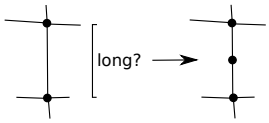

    IF there are loose mass points (only 3 neighbors) at right and left neighboring vertical springs, **THEN**:
      add springs between new point and loose neighbors:

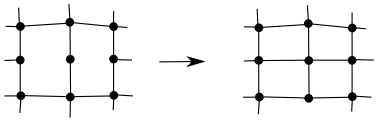

    ELSE
      add new mass points in middle of right or/and left neighboring vertical spring,
      add springs between new point and loose neighbors

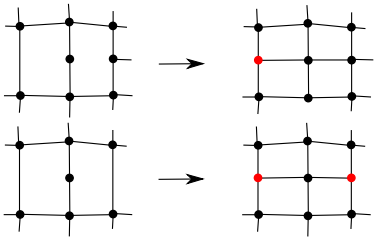

• new loose mass point

      count total number of new loose mass points (:= # new loose mass points)
    END IF
  END IF
  WHILE # new loose mass points > 0:
    "repair unit cells" -> not more than one loose mass point per unit cell:
    IF: **THEN:**

      # new loose mass points = # new loose mass points - 1
    ELSE IF: **THEN:**

    ELSE IF: **THEN:**

      # new loose mass points = # new loose mass points - 1
    ELSE
      # new loose mass points = # new loose mass points - 1
    END IF
  END WHILE
END FOR
FOR each horizontal spring: proceed similarly as for vertical springs: **END FOR**

Figure 3. Illustration of remeshing algorithm. Dots: mass points, lines: springs.

bioRxiv preprint doi: https://doi.org/10.1101/459412; this version posted November 1, 2018. The copyright holder for this preprint (which was not certified by peer review) is the author/funder, who has granted bioRxiv a license to display the preprint in perpetuity. It is made available under aCC-BY-NC 4.0 International license.

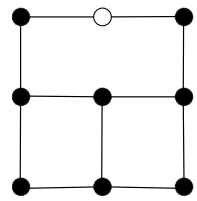

Figure 4. Illustration of usage of auxiliary point to calculate hinge strain for a loose mass point. The auxiliary point (white dot) is located in the middle of a spring between next-next neighbors Filled dots: mass points, black lines: springs.

where $h\gamma = 0.01$ is the dimensionless Verlet integration time step and γ is the integration time. For the initial time step

$$\boldsymbol{i}(0 + h\gamma) = \boldsymbol{i}(0) + \frac{1}{2}\frac{d^2}{d\gamma^2}\boldsymbol{i}(0) \times (h\gamma)^2$$

is used. The acceleration of a mass point i is found for each time step with

$$\frac{d^2}{d\gamma^2}\boldsymbol{i}(\gamma) = \frac{\boldsymbol{f}_i(\gamma)}{m},$$

where $m = 1\mu g$ is the mass of a mass point. The velocity of a mass point (to calculate the viscous force) in Eq.25 is computed with

$$\frac{d}{d\gamma}\boldsymbol{i}(\gamma) = \frac{\boldsymbol{i}(\gamma) - \boldsymbol{i}(\gamma - h\gamma)}{h\gamma}.$$

For Euler integration of the growth equation (Eq.27) we used an integration time step of $ht = 1\ min$. The resting distances of springs connected to a mass point after a growth step are computed with

$$\begin{bmatrix} x_0 \\ y_0 \end{bmatrix}(t + ht) = \left(1 + ht \begin{bmatrix} k_x^{rate} \\ k_y^{rate} \end{bmatrix}(t)\right) \begin{bmatrix} x_0 \\ y_0 \end{bmatrix}(t),$$

where t is the simulation time in minutes.

We solve the model as follows: from each time integration step of the growth model (Eq.27) a new set of resting distances of springs is obtained, which is passed on to the elasticity part of the model, where forces are computed (Eqs. 18,24,25), and the equations for the motion of the mass points (Eqs. 26) are solved, until the sum of forces on every mass point is below the convergence threshold $thr = 0.05\ \mu N$.

In this study we used model setups of initially rectangular meshes of various lengths. As initial resting lengths of springs 1 μm was used. To compute viscous forces (Eq. 25) $\eta = 1\ N \times h\gamma/\mu m$ was used as a damping constant. Several boundary conditions were used. For simulations shown in the results section a free floating medium (no degree of freedom is restrained, all mass points move freely) is used. In this setup a rigid body translation and rotation can occur; however, to display the model a linear transformation was employed (display in moving frame of reference) to cancel these out rigid body motions. In addition, in simulations to characterize the material properties of the model we either fix all boundaries of the model, or restrain points on specific boundaries to move on a line.

We set the parameter values of the model to connect it to experimental data on the model plant *Arabidopsis thaliana*. In experiments on roots, in which a rapid local growth was induced, a maximal relative elemental growth rate of one third per hour has been measured [48]. This corresponds to a

bioRxiv preprint doi: https://doi.org/10.1101/459412; this version posted November 1, 2018. The copyright holder for this preprint (which was not certified by peer review) is the author/funder, who has granted bioRxiv a license to display the preprint in perpetuity. It is made available under aCC-BY-NC 4.0 International license.

maximal growth rate $k_{max}^{rate} = ln(4/3)/60\ min^{-1} \approx 0.0048\ min^{-1}$, which we use as an upper boundary. In addition, we used as material properties Young's moduli in the range of $[20; 80]\ MPa \cdot m$, similar to reported experimental data on cell walls [49] and previous modeling work [27]. We varied turgor pressure in a range of $[0; 1]\ MPa \cdot m$, corresponding to values measured on the root [50]. There are to our knowledge no precise measurements of the Poisson ratio ν of the primary cell wall. However, it is established that the primary plant cell wall is a partially compressible material ($\nu < 0.5$) [51]. Previous modeling work [27] assumed $\nu = 0.2$. We vary ν in a range of $[0.1; 0.5]$ for simulations characterizing the model's material properties, and use $\nu = 0.2$ for simulations in the results section.

Characterization of material properties

Here we characterize how finite strain and plastic growth affects the material properties of our model in numerical simulations.

Effect of finite strain on material properties

We start with illustrating the effect of finite strain on material properties in an isotropic ($Y_x = Y_y = 20\ MPa; \nu = 0.1$) setup without turgor pressure. We show the results in Figure 5. In Figure 5A,top we illustrate the setup of the direct stress experiment. We applied uniform, direct stress to the upper boundary of the model, while the bottom of the model was kept fixed on a horizontal line. Figure 5A, middle shows a stress-strain plot of the direct-stress experiment (black line) and as a comparison the theoretical behavior of a material which follows Hooke's law (red line). We see that for small stress the model's behavior converges to the theoretical value. For increasing stress however, the model stiffens, and a higher direct stress is required to stretch the model. Figure 5A, bottom shows the apparent Young's modulus and Poisson ratio against the strain (ϵ_{yy}). We see that the Young's modulus (solid line) increases linearly with increasing strain (with slope $\approx 2\ MPa \cdot m/10\%$), while the Poisson ratio maintains its theoretical value (dotted line). Note that with the highest direct strain value of 5% applied in the result section of this paper, the model's Young's modulus is $\approx 5\%$ larger than that for a theoretical isotropic Hooke's material (without turgor). The linear increase in the stiffness of our simulated plant tissue is likely a result of our approximation to disregard the derivative of surface area A against strain (in Eq.8), which results in an error scaling linearly with direct strain (see Appendix **B** [39]).

Next, we tested the shear properties of the model. In Figure 5B,top we illustrate the setup of this experiment. We applied shear stress S_{xy} and S_{yx} of same strength. Figure 5B, middle shows a stress-strain plot of the shear-stress experiment (black line) and as a comparison the theoretical behavior of a material which follows Hooke's law (red line). We see that for smaller stress the model's behavior converges to the theoretical value. For increasing stress however, again the model stiffens. Figure 5B, bottom shows the apparent shear modulus μ_{model} against the strain (ϵ_{yy}). We see that the shear modulus increases non-linearly with increasing strain. For a substantial total shear strain of $\tau = 10\ \%$ the shear modulus stiffens 1 % compared to the theoretical value. Note that for the highest total shear strain of 5% which we chose as largest strain value in this paper, the model's shear modulus is $\approx 0.3\%$ larger than that following from the theoretical isotropic Hooke's material (without turgor). This non-linear increase in the stiffness is likely also a result from our approximation to disregard the derivative of A with respect to strain. We showed in Appendix **B** [39] that with respect to shear this approximation causes an error which scales quadratically with shear strain.

Next the isotropy of our model in an experiment illustrated in Figure 5C, top was measured. The rotating force, whose amplitude increases every rotation, was applied at the center point of a simulated tissue whose boundaries are fixed. To rule out boundary effects, we compared results of a medium of double the side length, and found qualitatively similar results (data not shown). Figure 5C, middle

bioRxiv preprint doi: https://doi.org/10.1101/459412; this version posted November 1, 2018. The copyright holder for this preprint (which was not certified by peer review) is the author/funder, who has granted bioRxiv a license to display the preprint in perpetuity. It is made available under aCC-BY-NC 4.0 International license.

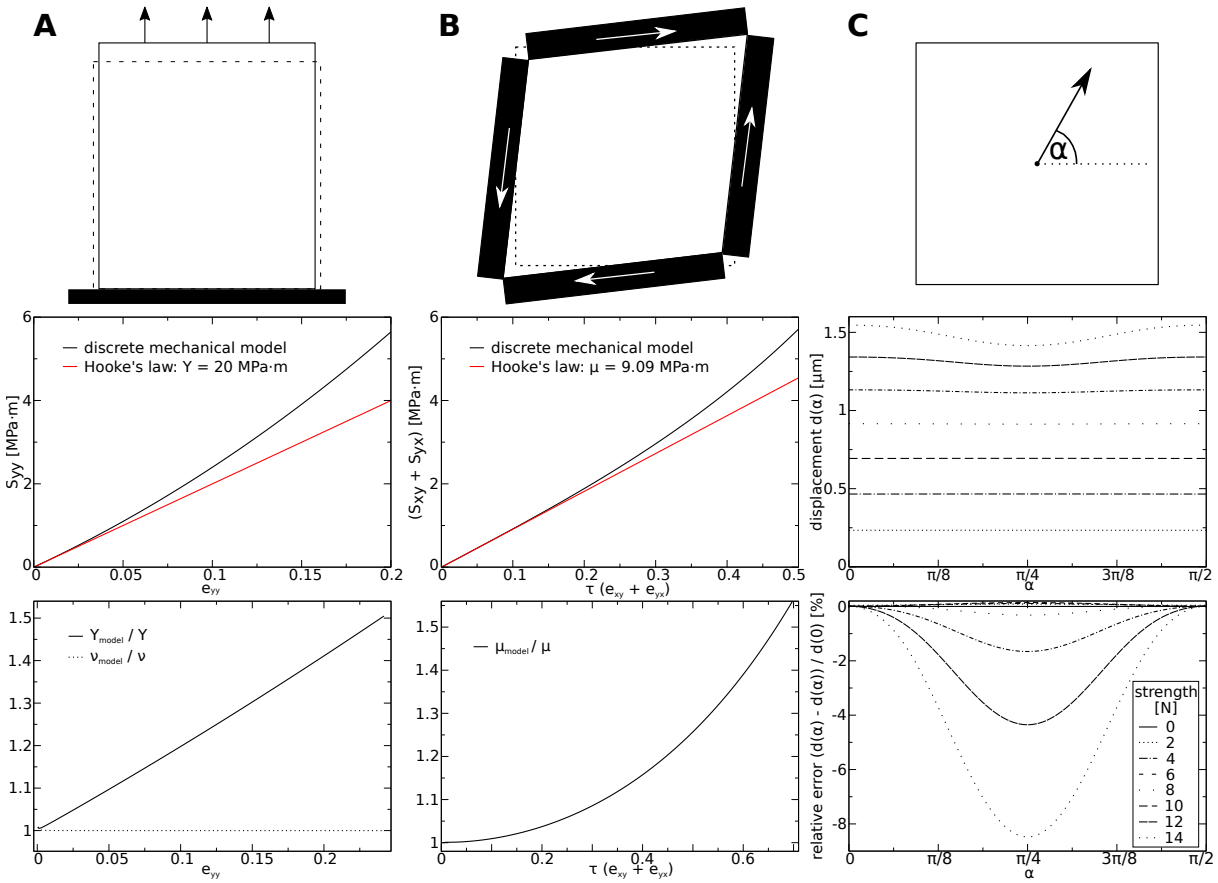

Figure 5. Illustration of material properties (isotropic, without turgor pressure). Top: Setups. Contours indicate undeformed (dotted) and deformed medium. Big arrows in **(A)** and **(B)** indicate applied stress. **(A) Direct stress experiment**. Top: Setup. Medium is fixed at the bottom (black block), such that points at lower border can only move horizontally. Middle: stress-strain plot. Bottom: ratio between the apparent and theoretical values (Y_{model}/Y, ν_{model}/ν) as a function of ϵ_{yy}. **(B) Pure shear stress experiment**. Top: Setup. Black blocks indicate walls through which shear stress is applied. Middle: stress-strain plot. Bottom: ratio between apparent shear modulus μ_{model} and theoretical μ as a function of τ. **(C) Isotropy experiment**. Top: Setup. Contour indicates fixed boundary of medium. Arrow symbolizes rotating force. Middle: displacement of center point for different strengths of force *vs* angle of force vector α. Length of undeformed squared medium 100 μm.

depicts the displacement of the center point against the strength and the angle of the applied force. It reveals that that for forces smaller than 10 N the relative error of the mass point's trajectory are smaller than 2%. However, it also shows that larger forces on the center mass point cause a substantial artificial anisotropy (error larger than 4%) in the model. A maximal strength of 14 N was applied in this study to the center point, which results in a substantial deformation gradient in the model. Note that this strength of force, if applied at all the boundary points, would correspond to a hydrostatic pressure of 14 $MPa \cdot m$ which is one magnitude larger as the turgor pressure typically measured in *Arabidopsis thaliana* [50]. From Figure 5C, bottom we show the deviation from isotropic behavior against the strength and the angle of the applied force. We see that for forces smaller than 12 N the error is smaller than 4 %, and

bioRxiv preprint doi: https://doi.org/10.1101/459412; this version posted November 1, 2018. The copyright holder for this preprint (which was not certified by peer review) is the author/funder, who has granted bioRxiv a license to display the preprint in perpetuity. It is made available under aCC-BY-NC 4.0 International license.

that for stronger forces the error substantially increases. In the simulations in the results section of this paper such localized strong forces do not occur, and thus we think that the model approximates the generalized Hooke's law well.

Effect of turgor pressure and anisotropy: We also studied the effect of finite strain on material properties in presence of turgor pressure and elastic anisotropy. Due to space limitations we put this extended characterization in the Supplemental Material [39], and give here only a short summary. Turgor pressure p_t increases the elastic moduli linearly. We predict analytically, and measure numerically for the apparent shear modulus $\mu_{\text{model}} \approx 4 \times p_t + \mu$, and for the apparent Young's modulus $Y_{\text{model}} \approx 2 \times p_t + Y$. We found numerically that the Poisson ratio is not affected significantly by p_t. In presence of turgor pressure ($0.5\ MPa \cdot m$) and elastic anisotropy, we found that the material properties of the medium are well characterized by the generalized orthotropic material law (Eq. 15).

Effect of plastic growth on material properties

Above we demonstrated how the model's material properties are affected by finite strain. Here show show how plastic growth affects the material properties of the model. First similar experiments as shown above were performed, applying direct or shear stress while letting the medium grow uniformly. We show the results in Figure 6A-C. It can be seen from Figure 6A and B that Y and ν are affected little by plastic

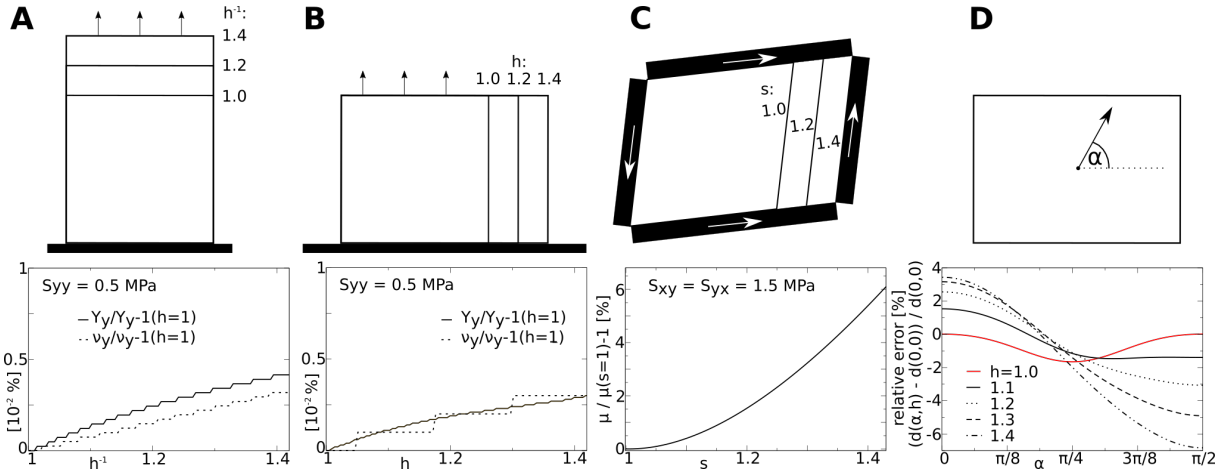

Figure 6. Material properties during growth. Fine lines indicate different system sizes (for different metric terms h and s). **(A) Direct stress experiment - growth in y-direction**. Top: Setup. Medium is fixed at the bottom (black block), such that points at lower border can move only horizontally. Black arrows indicate direct stress. Bottom: relative error of Young's modulus and Poisson's ratio as a function of h^{-1}. **(B) Direct stress experiment - growth in x-direction**. similar to subfigure (A). **(C) Pure shear stress experiment**. Top: Setup. Black blocks indicate walls through which shear stress is applied. White arrows indicate shear stress (all same strength). Bottom: shear modulus as a function of s. **(D) Isotropy experiment**. Top: Setup. Contour indicates fixed boundary of medium (for $h = 1.4$). Arrow symbolizes rotating force. Bottom: error of trajectories for different h relative to displacement for $\alpha = 0$, and $h = 1.0$. Length of initial ($h = 1.0$) squared medium 100 μm.

growth, for an increase from $h = 1$ (or $h^{-1} = 1$) to the maximal value of $\sqrt{2}$ (when remeshing happens) changes in these material properties are less than 0.01%. However, from Figure 6C we can see that the

bioRxiv preprint doi: https://doi.org/10.1101/459412; this version posted November 1, 2018. The copyright holder for this preprint (which was not certified by peer review) is the author/funder, who has granted bioRxiv a license to display the preprint in perpetuity. It is made available under aCC-BY-NC 4.0 International license.

shear modulus is affected substantially by plastic growth, it changes $\approx 6\%$, when s is increased from 1 to the maximal value of $\sqrt{2}$. Moreover, the isotropy experiment (compare to Figure 5C) was repeated in a medium which we first let grow in horizontal direction. We show the relative error of trajectories of the center mass point (to which the rotating force is applied) for different values of h, and a strong local force of 10 N (compare Figure 5C). We find that the maximal change in metric of the unit cells due to growth causes a maximal relative error of $\approx 7\%$ (compared to ideal circular trajectory).

We can conclude that growth causes a change in the metric of unit cells in our model, and that these changes affect the material properties mainly in its shear modulus. This artifact also manifests as a deviation from the ideal isotropic behavior.

Results

As a first application of our model we studied emergent residual strain fields and bulk tissue deformation that arise due to anisotropic growth in rectangular model setups. We show data where a maximal residual strain of 5% emerges in the tissue, similar to previous modeling work [27].

Anisotropic elongation: "root bending"

An important phenomenon in plant development is the bending of the root, for instance to grow towards nutrients, or to follow the gravitational field. Such directional growth responses are called tropisms, and they arise from a directional environmental signal becoming translated into a tissue level asymmetry of the plant hormone auxin. Since auxin levels dictate cellular expansion rates, this auxin asymmetry subsequently induces a growth rate asymmetry that results in bending. To illustrate the application of our method to the study of tropisms we here simply superimposed a growth rate asymmetry.

To model root tropism, we use a slab of tissue with initial size 76 $\mu m \times 32$ μm, with Young's moduli $Y_x = 40$ $MPa \cdot m$ and $Y_y = 80$ $MPa \cdot m$, Poisson's ratio $\nu = 0.2$ and turgor pressure $p_t = 0.2$ $MPa \cdot m$. We show the results of the simulation in Figure 7 and in a Supplemental movie [39]. Growth happens in this setup only in x-direction (elongation along the "root axis"), and an asymmetric growth field is used (see Figure 7, second column) such that the upper part of the "root" grows faster than the lower part. We see that the asymmetric growth causes a bending of the tissue, where the inner side of the arc is the side with the slower growth rate. At 42 min the onset of bending can be seen. For time points 85 and 107 min a slight negative strain (compression) in the x-direction emerges (third column), which is weaker at the ends of the medium. In these snapshots we also see that remeshing is happening (left column) due to the growth process, starting from the outside arc, the location of highest growth rate and "propagating as a wave" towards the inner side of the arc. This remeshing does not cause a visible disruption of the direct strain in the x-direction (third column); however, for the absolute shear (right column) we see that the remeshing causes a slight local distortion of the shear strain field (see thin red line). These effects of the remeshing on the strain fields can be explained by our findings shown in Figure 6, where we showed that plastic growth affects the shear modulus, but hardly affects the Young's modulus. Later the simulation (129, and 141 min) shows that the negative strain in the x-direction increases at the inner side of the arc (where the growth rate is smaller) to a maximum of -5%, whereas the strain on the fast growing side (outer side of the arc) is minimal. Furthermore we can see the emergence of a substantial shear strain field (see two "red eyes" in the right column). Note that throughout the simulation strain in the y-direction was very small, which is why we choose to not show it in Figure 7 (it is included in the Supplemental movie).

bioRxiv preprint doi: https://doi.org/10.1101/459412; this version posted November 1, 2018. The copyright holder for this preprint (which was not certified by peer review) is the author/funder, who has granted bioRxiv a license to display the preprint in perpetuity. It is made available under aCC-BY-NC 4.0 International license.

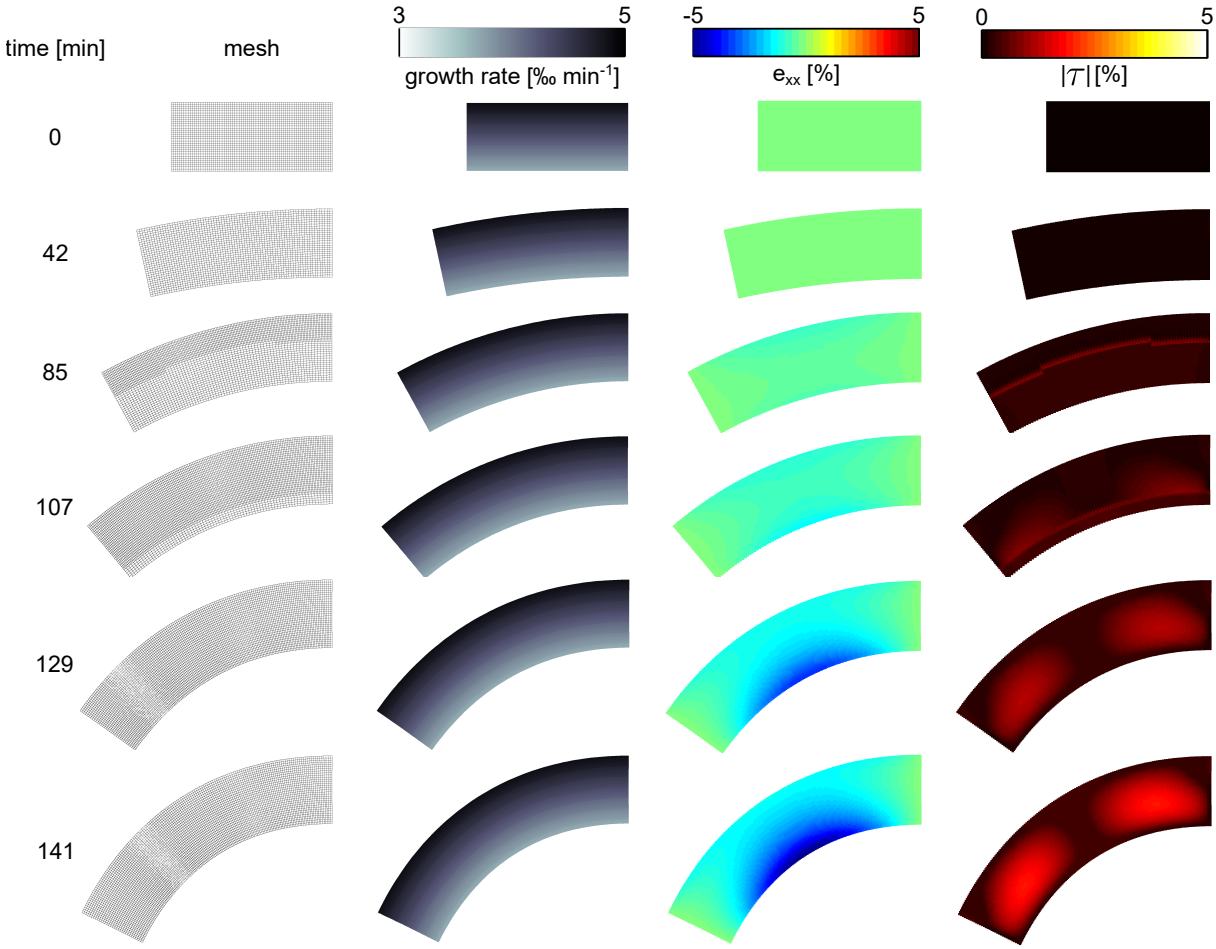

Figure 7. Application "root bending". Anisotropic elongation (growth along root axis) causes emergence of residual strain fields and bending of the bulk tissue.

Anisotropic growth in two dimensions "leaf growth"

In many plant tissues, plastic growth is not restricted to a single direction. For example in leaf blades, tissue growth happens in two principal directions. Additionally, in case of bidirectional growth, tissue expansion is often anisotropic. Here we demonstrate such differential bidirectional growth in our model. For this we consider an initially quadratic slab of tissue with initial size 76 $\mu m \times 67\ \mu m$, with Young's moduli $Y_x = 40\ MPa \cdot m$ and $Y_y = 80\ MPa \cdot m$, Poisson's ratio $\nu = 0.2$ and turgor pressure $p_t = 0.2\ MPa \cdot m$. We show the results of this simulation in Figure 8 and in a Supplemental movie [39]. We apply growth in both directions, and use an asymmetric growth field (see Figure 8, second column). We see that residual strain fields emerge in the growing tissue. From Figure 8, third column we see that during growth positive strain in x-direction (stretch) gradually increases at the upper and lower border of the tissue, whereas a negative strain in the x-direction emerges in the center of the medium. In contrast to strain in the x-direction, in the y-direction weaker positive strain at the left and right borders gradually increases during growth, and no compression strain in the center happens. This can partly be explained by the elastic anisotropy of the tissue, where the stiffness in y-direction is twice larger compared to the

bioRxiv preprint doi: https://doi.org/10.1101/459412; this version posted November 1, 2018. The copyright holder for this preprint (which was not certified by peer review) is the author/funder, who has granted bioRxiv a license to display the preprint in perpetuity. It is made available under aCC-BY-NC 4.0 International license.

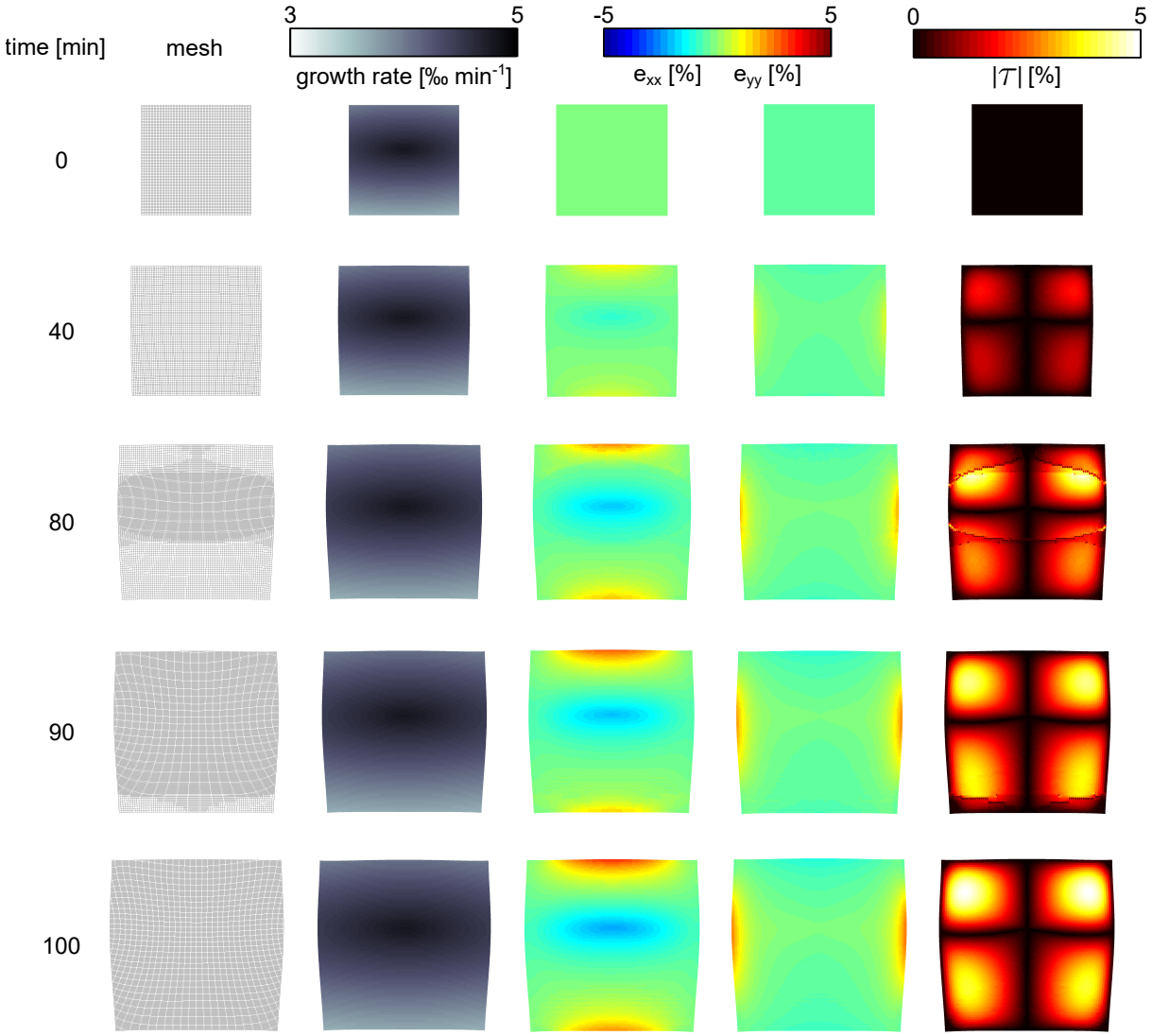

Figure 8. Application differential growth in 2D "leaf growth". Anisotropic growth (in both directions) causes emergence of residual strain fields in the tissue.

x-direction (compare Figure 8, fourth column) causing that the tissue is easier deformed in x-direction than y-direction. We see that a substantial shear strain field (see four "red eyes" in right column) emerges in the medium.

Discussion

We introduced a discrete mechanical growth model to study plant growth and development. The model contains an orthogonally organized mesh of mass points and connecting springs, providing an intuitive resemblance to the typical orthogonal microfibril architecture of anisotropic, polarized plant cells. We

bioRxiv preprint doi: https://doi.org/10.1101/459412; this version posted November 1, 2018. The copyright holder for this preprint (which was not certified by peer review) is the author/funder, who has granted bioRxiv a license to display the preprint in perpetuity. It is made available under aCC-BY-NC 4.0 International license.

approximate the model's material properties as an orthotropic Hookean material. The discrete nature of the method enables the incorporation of experimental data on material properties on subcellular level. Compared to continuous mechanics approaches our method is relatively easy to implement in a computationally efficient manner, and allows usage of "simpler" integration schemes. We propose the method as a building block for multi-process models. Researchers can link gene regulation, hormonal signaling, water transport and cellular behavior to the mechanics of tissue growth and deformation.

The model was used to study the consequences of growth. We found that anisotropic growth causes emergent strain fields in the medium, and that an asymmetric elongation (similar to root growth) causes a bending of the bulk tissue. It would be interesting to compare our predictions regarding tissue bending and emergence of strain fields to continuum mechanics models, and test them experimentally. Thusfar, the role of strain fields in root tropisms has not been investigated. Potentially the feedback of strain on growth mechanics could play a role in regulating growth asymmetry.

The model's material properties were characterized in a series of simulations, and discussed deviations from the approximated material law that arise from finite strain and plastic growth. A further limitation regarding material properties emerges from our choice of the coordinate system (fiber directions) to couple the discrete method to a continuous material. In presence of shear the underlying coordinate system is not ideally orthogonal but skewed. If under such conditions direct stress is applied, the "Poisson effect" in the model will artificially cause a force which is not perfectly orthogonal to the stress, but skewed. Importantly, for multi-scale biological models, the aim is to uncover how interactions between different processes shape tissue growth, development and adaptation rather than making precise predictions. In addition, typically, such research requires large numbers of exploratory simulations that probe different possible interactions between processes, initial conditions and parameter regimes, as opposed to computing a few distinct scenarios. Thus, we argue that the high computational efficiency and ease of use of the mechanics module developed here, outweighs its limitations in terms of accuracy for the aims it was developed for.

The model can be extended in various directions. For example, because of the discrete nature of the method breakage of cell wall material can be modeled with a removal of mass points, springs and hinges. This can be useful to model lateral root emergence when the forming tissue breaks through upper cell layers. In this paper we used simple growth functions to illustrate the model. However, as a next step growth should be formulated in terms of physiological processes. For instance, local growth can be formulated in terms of local auxin concentrations, strain fields and cytoskeletal processes. Moreover, the method may be applied not only to study plant tissue, but also to study other turgoid cell types of bacteria or fungi.

Availability

The model was implemented using the C and C++ programming languages. The current version of the source code is available as Supplemental Material [39]. The software uses the Intel threading building blocks (TBB) runtime library as a parallelization environment (available in open source from [52]), and for visualization the CASH library from Rob J. de Boer and Alex D. Staritsky (available in open source from [53]).

bioRxiv preprint doi: https://doi.org/10.1101/459412; this version posted November 1, 2018. The copyright holder for this preprint (which was not certified by peer review) is the author/funder, who has granted bioRxiv a license to display the preprint in perpetuity. It is made available under aCC-BY-NC 4.0 International license.

Conflict of interest statement

The authors declare that the research was conducted in the absence of any commercial or financial relationships that could be construed as a potential conflict of interest.

Author contributions statement

KT conceived and planned the research. LW developed the model, implemented the software, performed the analytic calculations and numerical simulations. LW and KT wrote the manuscript.

Acknowledgements

We thank Dr. Michael Sheinman, Sander Arens, Dr. Nadya Timofeeva, Dr. Matthias Mimault, Laurens Kreh, and Dr. Chris van Dorp for valuable discussions and critical comments on the manuscript. We thank Dr. Paul Baron for help with language editing of the manuscript and Jan Kees van Amerongen for excellent technical support. This research is funded by the Netherlands Organization for Scientific Research (NWO Grant No. 864.14.003).

References

1. Thimann KV (1935) On the Plant Growth Hormone Produced by Rhizopus Suinus. Journal of Biological Chemistry 109: 279–291.

2. Vieten A, Vanneste S, Wiśniewska J, Benková E, Benjamins R, et al. (2005) Functional redundancy of PIN proteins is accompanied by auxin-dependent cross-regulation of PIN expression. Development 132: 4521–4531.

3. Blilou I, Xu J, Wildwater M, Willemsen V, Paponov I, et al. (2005) The PIN auxin efflux facilitator network controls growth and patterning in *Arabidopsis* roots. Nature 433: 39.

4. Gray WM (2004) Hormonal Regulation of Plant Growth and Development. PLoS Biology 2: e311.

5. Choi D, Lee Y, Cho HT, Kende H (2003) Regulation of Expansin Gene Expression Affects Growth and Development in Transgenic Rice Plants. The Plant Cell 15: 1386–1398.

6. Sampathkumar A, Yan A, Krupinski P, Meyerowitz EM (2014) Physical forces regulate plant development and morphogenesis. Current biology 24: 475–483.

7. Kierzkowski D, Nakayama N, Routier-Kierzkowska AL, Weber A, Bayer E, et al. (2012) Elastic Domains Regulate Growth and Organogenesis in the Plant Shoot Apical Meristem. Science 335: 1096–1099.

8. Grieneisen VA, Xu J, Marée AFM, Hogeweg P, Scheres B (2007) Auxin transport is sufficient to generate a maximum and gradient guiding root growth. Nature 449: 1008-1013.

9. Vanneste S, Friml J (2009) Auxin: A Trigger for Change in Plant Development. Cell 136: 1005–1016.

10. Laskowski M, Grieneisen VA, Hofhuis H, ten Hove CA, Hogeweg P, et al. (2008) Root System Architecture from Coupling Cell Shape to Auxin Transport. PLOS Biology 6: e307.

bioRxiv preprint doi: https://doi.org/10.1101/459412; this version posted November 1, 2018. The copyright holder for this preprint (which was not certified by peer review) is the author/funder, who has granted bioRxiv a license to display the preprint in perpetuity. It is made available under aCC-BY-NC 4.0 International license.

11. Ditengou FA, Teale WD, Kochersperger P, Flittner KA, Kneuper I, et al. (2008) Mechanical induction of lateral root initiation in Arabidopsis thaliana. Proceedings of the National Academy of Sciences 105: 18818–18823.

12. Hogeweg P (2009) Multilevel Modeling of Morphogenesis. In: Corne DW, Frisco P, Păun G, Rozenberg G, Salomaa A, editors, Membrane Computing: 9th International Workshop, WMC 2008, Edinburgh, UK, July 28-31, 2008, Revised Selected and Invited Papers, Berlin, Heidelberg: Springer Berlin Heidelberg. pp. 29–35.

13. Grieneisen VA, Scheres B (2009) Back to the future: evolution of computational models in plant morphogenesis. Current Opinion in Plant Biology 12: 606–614.

14. Mähönen AP, ten Tusscher K, Siligato R, Smetana O, Díaz-Triviño S, et al. (2014) PLETHORA gradient formation mechanism separates auxin responses. Nature 515: 125.

15. Hamant O, Heisler MG, Jönsson H, Krupinski P, Uyttewaal M, et al. (2008) Developmental Patterning by Mechanical Signals in Arabidopsis. Science 322: 1650–1655.

16. Merks RMH, Guravage M, Inz D, Beemster GTS (2011) VirtualLeaf: An open-source framework for cell-based modeling of plant tissue growth and development. Plant Physiology 155: 656–666.

17. Fozard JA, Lucas M, King JR, Jensen OE (2013) Vertex-element models for anisotropic growth of elongated plant organs. Frontiers in Plant Science 4.

18. Fozard JA, Bennett MJ, King JR, Jensen OE (2016) Hybrid vertex-midline modelling of elongated plant organs. Interface Focus 6.

19. Hamant O, Haswell ES (2017) Life behind the wall: sensing mechanical cues in plants. BMC Biology 15.

20. Louveaux M, Julien JD, Mirabet V, Boudaoud A, Hamant O (2016) Cell division plane orientation based on tensile stress in Arabidopsis thaliana. Proceedings of the National Academy of Sciences 113: E4294–E4303.

21. Hejnowicz n, Rusin n, Rusin n (2000) Tensile Tissue Stress Affects the Orientation of Cortical Microtubules in the Epidermis of Sunflower Hypocotyl. Journal of Plant Growth Regulation 19: 31–44.

22. Jensen OE, Fozard JA (2015) Multiscale Models in the Biomechanics of Plant Growth. Physiology 30: 159–166.

23. Barbez E, Dünser K, Gaidora A, Lendl T, Busch W (2017) Auxin steers root cell expansion via apoplastic pH regulation inArabidopsis thaliana. Proceedings of the National Academy of Sciences of the United States of America 114: E4884–E4893.

24. Kumpf RP, Shi CL, Larrieu A, Stø IM, Butenko MA, et al. (2013) Floral organ abscission peptide IDA and its HAE/HSL2 receptors control cell separation during lateral root emergence. Proceedings of the National Academy of Sciences of the United States of America 110: 5235–5240.

25. Ali O, Mirabet V, Godin C, Traas J (2014) Physical models of plant development. Annual Review of Cell and Developmental Biology 30: 59–78.

26. Hamant O, Traas J (2010) The mechanics behind plant development. New Phytologist 185: 369–385.

bioRxiv preprint doi: https://doi.org/10.1101/459412; this version posted November 1, 2018. The copyright holder for this preprint (which was not certified by peer review) is the author/funder, who has granted bioRxiv a license to display the preprint in perpetuity. It is made available under aCC-BY-NC 4.0 International license.

27. Bozorg B, Krupinski P, Jönsson H (2014) Stress and Strain Provide Positional and Directional Cues in Development. PLOS Computational Biology 10: e1003410.

28. Weise LD, Panfilov AV (2015) Discrete Mechanical Modeling of Mechanoelectrical Feedback in Cardiac Tissue: Novel Mechanisms of Spiral Wave Initiation. In: Quarteroni A, editor, Modeling the Heart and the Circulatory System, Springer International Publishing, number 14 in MS&A. pp. 29–50.

29. Bozorg B, Krupinski P, Jönsson H (2016) A continuous growth model for plant tissue. Physical Biology 13: 065002.

30. Niklas KJ, Paolillo DJ (1997) The role of the epidermis as a stiffening agent in Tulipa (Liliaceae) stems. American Journal of Botany 84: 735–744.

31. Kutschera U, Niklas KJ (2007) The epidermal-growth-control theory of stem elongation: An old and a new perspective. Journal of Plant Physiology 164: 1395–1409.

32. Gibson LJ (2012) The hierarchical structure and mechanics of plant materials. Journal of The Royal Society Interface 9: 2749–2766.

33. Radoti K, Roduit C, Simonovi J, Hornitschek P, Fankhauser C, et al. (2012) Atomic Force Microscopy Stiffness Tomography on Living Arabidopsis thaliana Cells Reveals the Mechanical Properties of Surface and Deep Cell-Wall Layers during Growth. Biophysical Journal 103: 386–394.

34. Vogler H, Felekis D, Nelson BJ, Grossniklaus U (2015) Measuring the Mechanical Properties of Plant Cell Walls. Plants 4: 167–182.

35. Weber A, Braybrook S, Huflejt M, Mosca G, Routier-Kierzkowska AL, et al. (2015) Measuring the mechanical properties of plant cells by combining micro-indentation with osmotic treatments. Journal of Experimental Botany 66: 3229–3241.

36. Saxe F, Eder M, Benecke G, Aichmayer B, Fratzl P, et al. (2014) Measuring the distribution of cellulose microfibril angles in primary cell walls by small angle X-ray scattering. Plant Methods 10: 25.

37. Feynman R, Leighton R, Sands M (1969) Feynman lectures on physics: mainly electromagnetism and matter. Massachusetts, New York. USA: Addison-Wesley. 592 p.

38. Landau LD, Lifshitz EM (1975) Theory of elasticity, volume 7 of Course of Theoretical Physics. Oxford, United Kingdom: Pergamon Press.

39. Find supplemental data on http://link-to-si/.

40. Meyers M, Chawla K (2009) Mechanical Behavior of Materials, 2nd edition. New York, USA: Cambridge University Press.

41. Eringen A (1980) Mechanics of Continua. New York: Krieger.

42. Biot M (1939) Non-linear theory of elasticity and the linearized case for a body under initial stress. Philosophical Magazine and Journal of Science 27: 468-489.

43. Seth B (1964) Generalized strain measure with applications to physical problems. In: Reiner M, Abir D, editors, Second-order effects in elasticity, plasticity and fluid dynamics. Oxford, UK: Pergamon, pp. 162-172.

44. Braden B (1986) The Surveyor's Area Formula. The College Mathematics Journal 17: 326–337.

bioRxiv preprint doi: https://doi.org/10.1101/459412; this version posted November 1, 2018. The copyright holder for this preprint (which was not certified by peer review) is the author/funder, who has granted bioRxiv a license to display the preprint in perpetuity. It is made available under aCC-BY-NC 4.0 International license.

45. Cosgrove DJ (2005) Growth of the plant cell wall. Nature Reviews Molecular Cell Biology 6: 850.

46. Yavari A (2010) A Geometric Theory of Growth Mechanics. Journal of Nonlinear Science 20: 781–830.

47. Verlet L (1967) Computer "experiments" on classical fluids. i. thermodynamical properties of lennard-jones molecules. Phys Rev 159: 98.

48. Mullen JL, Ishikawa H, Evans ML (1998) Analysis of changes in relative elemental growth rate patterns in the elongation zone of Arabidopsis roots upon gravistimulation. Planta 206: 598–603.

49. Ryden P, Sugimoto-Shirasu K, Smith AC, Findlay K, Reiter WD, et al. (2003) Tensile Properties of Arabidopsis Cell Walls Depend on Both a Xyloglucan Cross-Linked Microfibrillar Network and Rhamnogalacturonan II-Borate Complexes. Plant Physiology 132: 1033–1040.

50. Shabala SN, Lew RR (2002) Turgor Regulation in Osmotically Stressed Arabidopsis Epidermal Root Cells. Direct Support for the Role of Inorganic Ion Uptake as Revealed by Concurrent Flux and Cell Turgor Measurements. Plant Physiology 129: 290–299.

51. Chanliaud E, Burrows KM, Jeronimidis G, Gidley MJ (2002) Mechanical properties of primary plant cell wall analogues. Planta 215: 989–996.

52. http://www.intel.com/software/products/tbb/.

53. http://theory.bio.uu.nl/rdb/software.html.